Journal of Computational Science 30 (2019) 28–40

Contents lists available at ScienceDirect

Journal of Computational Science

journal homepage: www.elsevier.com/locate/jocs

# Sphericity and roundness computation for particles using the extreme vertices model

Irving Cruz-Matías [a,*], Dolors Ayala [b], Daniel Hiller [c], Sebastian Gutsch [d], Margit Zacharias [d], Sònia Estradé [e,f], Francesca Peiró [e,f]

[a] Computer Science Department, University of Monterrey, Mexico
[b] Computer Science Department, Polytechnical University of Catalonia, Spain
[c] Research School of Engineering, Australian National University, Canberra, Australia
[d] IMTEK, Faculty of Engineering, Albert-Ludwigs-University Freiburg, Freiburg, Germany
[e] LENS-MIND Laboratory of Electron Nanoscopies, Engineering Department: Electronics, University of Barcelone, Spain
[f] Institute of Nanoscience and Nanotechnology (In2UB), Barcelone, Spain

ARTICLE INFO

*Article history:*
Received 14 May 2018
Received in revised form 6 November 2018
Accepted 8 November 2018
Available online 13 November 2018

*Keywords:*
Binary volumes
Shape description
Length measurements
Oriented Bounding Box
Sphericity
Roundness

ABSTRACT

Shape is a property studied for many kinds of particles. Among shape parameters, sphericity and roundness indices had been largely studied to understand several processes. Some of these indices are based on length measurements of the particle obtained from its oriented bounding box (OBB). In this paper we follow a discrete approach based on Extreme Vertices Model and devise new methods to compute the OBB and the mentioned indices. We apply these methods to synthetic sedimentary rocks and to a real dataset of silicon nanocrystals (Si NC) to analyze the obtained results and compare them with those obtained with a classical voxel model.



## 1. Introduction

Computed-based experimentation is getting a growing interest in many fields where scientific data coming from real samples are used to compute structural parameters as porosity, connectivity, sphericity and roundness among others. In the bioengineering field, these parameters allow to evaluate physical properties such as the osteoporosis degree of bones [30] and the suitability of biomaterials to be used as implants [42]. In geology, they allow to analyze the transport and distribution of fluids into sedimentary rocks for petrographic purposes [33] and the grain shape and sphericity index in silica sand for industrial and manufacturing applications [40]. In the nanoscopy field, the size and sphericity of silicon nanocrystals are useful parameters to determine their applicability as optoelectronic materials [15,48] in Si based light emitters, as sensor material with optical readout, or as label material in bio-imaging.

In this work we focus on sphericity and roundness parameters. Sphericity is a measure of the degree to which a particle approximates the shape of a sphere, and is independent of its size. Roundness is the measure of the sharpness of a particle's edges and corners. They measure two different morphological properties: sphericity is most dependent on elongation, whereas roundness is largely dependent on the sharpness of angular protrusions (convexities) and indentations (concavities) from the object. Sphericity and roundness are ratios and, therefore, dimensionless numbers. Some of these indices are based on length measurements of the three representative axes of a reference ellipsoid of the particle that can be computed from its oriented bounding box.

The contribution of this paper is focused on rock-like objects as those shown in Figs. Fig. 11 and 5 (sand particles, pebbles or gravel) as well as on Si nanocrystals (NCs). The presented methodology performs well with these two types of objects although they have very different sizes which is a guaranty of its validity. They are 0-genus objects that may show protrusions and concavities and we are not restricted to star-shaped objects as in [9].

* Corresponding author.
*E-mail addresses:* irving.cruz@udem.edu (I. Cruz-Matías), dolorsa@lsi.upc.edu (D. Ayala), daniel.hiller@anu.edu.au (D. Hiller), sebastian.gutsch@imtek.uni-freiburg.de (S. Gutsch), zacharias@imtek.de (M. Zacharias).

https://doi.org/10.1016/j.jocs.2018.11.005

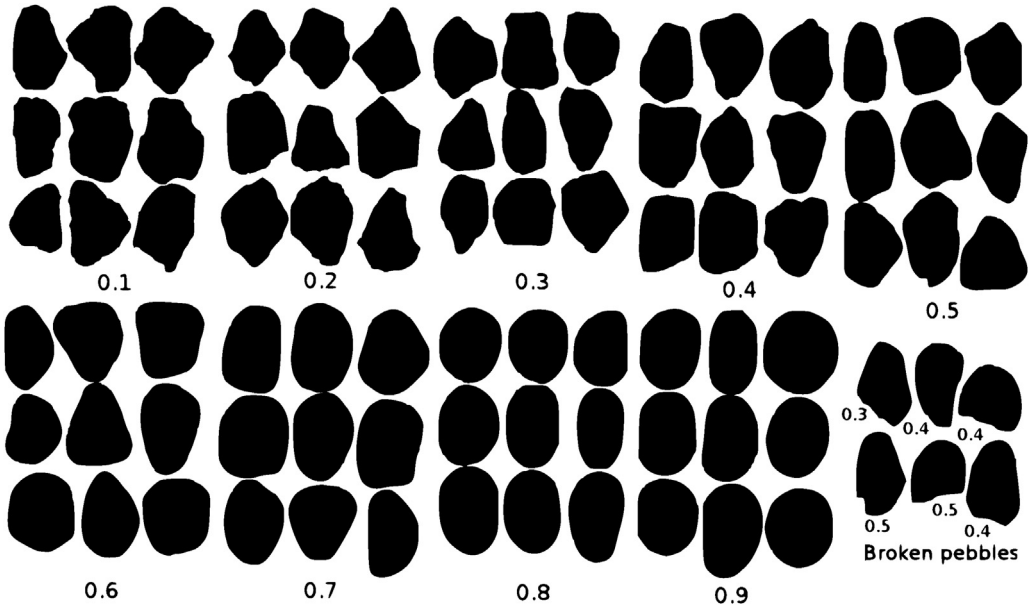


**Fig. 1.** Krumbein's chart for visual determination of roundness [26].

In most of the reported literature, the operations to study the structural parameters are performed directly on the classical voxel model. In this paper, we propose new geometric methods to compute sphericity and roundness based on the Extreme Vertices Model (EVM). EVM is a concise representation model for binary volumes and we have developed an EVM-based platform which offers a series of operations for binary volumes that have been used in the methods and results presented in this paper, as erosion, dilation and connected component labelling. The conversion cost from the initial voxel model (VXM) to EVM is shared by all of these operations. See Section 3. The main contributions of this paper are:

- Two EVM-based methods to compute the oriented bounding box (see Section 4.1) and a 3D roundness index (see Section 4.3).
- Results showing the efficiency and accuracy of the presented methods applied to two sets of data: a set of 30 synthetic rocks (Section 5) and a real Si NC dataset (Section 6).

This paper is based in part on the doctoral thesis by the corresponding author [10]. Here we improve and extend the obtained results. Concerning the rock dataset (Section 5), we present a discussion on the OBB volume obtained with VXM and EVM, a comparative between VXM and EVM model to compute the sphericity and roundness based on length measurements, and an analysis of how the resolution affects the computation of the OBB, sphericity and roundness indexes.

Concerning the results with a Si NC datasets, in a recent publication [23] an accurate description of the acquisition method and samples is presented and the obtained results concerning the computation of shape and true sphericity with VXM are validated by the NC experts. These results have encouraged us to further extend and improve this study by including an analysis of values of sphericity based on length measurements, true sphericity and roundness computed with VXM and EVM for this Si NC dataset (Section 6).

## 2. Related work

### 2.1. Sphericity

Sphericity is one of the most used compactness measure of a shape [49]. There are basically two formulation theories for the sphericity index. One of them is based on length measurements and the other one on the volume and surface area (true sphericity).

Length measurements are the lengths of the three representative axes of an object, $a = d_L$ (longest), $b = d_I$ (intermediate) and $c = d_S$ (shortest) and correspond to its OBB or reference ellipsoid. They can be computed by principal component analysis (PCA) on the corresponding voxel model [3,24].

There are several formulations of this type. A simplified sphericity index is defined as $\Psi = d_n/a$ [45], where $d_n$ is the nominal diameter (diameter of the sphere having the same volume as the object).

Krumbein defined the intercept sphericity as $\Psi = \sqrt[3]{bc/a^2}$ which is a function of the volume ratio of the reference ellipsoid to the circumscribing sphere. A more widely accepted sphericity index is [41]:

$$\Psi = \sqrt[3]{c^2/ab} \tag{1}$$

From these length measurements the three elongation parameters can be computed: $e_{yx} = b/a$, $e_{zx} = c/a$ and $e_{zy} = c/b$.

The so-called true sphericity index was defined by Wadell [44] as the ratio of the nominal surface area, $S_n$ (surface area of a sphere having the same volume as the object), to the actual surface area of the object, $S$:

$$\Psi = \frac{S_n}{S} = \frac{\sqrt[3]{36\pi V^2}}{S} \tag{2}$$

where $V$ is the volume of the object. The circularity index, $c = 4\pi S/perimeter^2$ is the 2D equivalent of the true sphericity index. Both indices range from 1 (perfect sphere or circle) to 0 (elongated shape).

Volume and surface are computed directly from the voxel model [4,24] by summing voxels and external surfels respectively. A better estimation of the surface area can be obtained by a weighted average of the boundary voxels [46] or extracting a triangulated mesh with MC (Marching Cubes) [29].

Other sphericity indices can be defined as $\Psi = V_p/V_s$ [3] where $V_p$ is the actual volume of the particle, computed summing voxels, and $V_s$ is the volume of a sphere with diameter $c$.

Approaches based on the continuum representation use spherical harmonic expansions to compute $S$ and $V$ [9,51].

Sphericity related indices have also been computed at nanoscopic scale. An equivalent spherical diameter is used to obtain a pore size distribution in nanoporous materials [18].

Si NCs are analyzed with 2D software, ImageJ, to obtain the equivalent diameter [19] and circularity index [28], and a 3D software, Amira, is used to compute size and Lent measurements [25] of quantum dot particles.

A different approach uses cross-correlation to adjust the three elongation parameters of the ellipsoid best fitting the particle [34].

Finally, another measure in use to compute the compactness is the convexity ($C_x$), which describes how closely a particle represents a convex hull and can be defined as $C_x = V/V_{CH}$, where $V$ is the volume of the particle and $V_{CH}$ the volume of the convex hull enclosing the particle [49].

### 2.2. Roundness

Although roundness is a 3D property, some methods work with the maximum 2D projection plane (silhouette) of the object looking for a trade-off between accuracy and time.

Roundness ($\mathcal{R}$) was defined by Wadell [44] as the ratio of the average radius of curvature of the corners of the object's silhouette to the radius of the maximum inscribed circle: $\mathcal{R} = (\frac{1}{n}\sum_{i=1}^{n} r_i)/r_{\max}$, where $n$ is the number of corners, $r_i$ the radius of the $i$th corner curvature, and $r_{max}$ the radius of the maximum inscribed circle. $\mathcal{R}$ is 1 for a perfectly round object and less than 1 for any other object.

The Krumbein chart (KC) [26] shows examples of pebbles for which the roundness has been calculated using this equation and grouped into nine classes (see Fig. 1).

2D methods can be based on granulometry (morphological opening) [14] or on discrete geometry (distance transform of the silhouette) [39]. They exhibit a correlation with KC of 0.96 and 0.92 respectively. A recent approach computes roundness [50] by fitting circles at the corners. There is also a ray-casting based approach [35]. In it, equally spaced rays are traced from the centre of a least-squares circle and the roundness is obtained as the average of distances $d_i - r$, where $d_i$ is the distance from the circle center to the intersection point between the $i$th ray and the object and $r$ is the radius of the circle.

There are 3D approaches following Wadell definition. From the voxel model, a MC triangulated mesh is computed and from them principal, mean and Gaussian curvatures can be estimated [49]. Another approach uses only the maximum principal curvature and computes it with spherical harmonic expansions [9]. Both approaches are very time consuming and the first one simplifies the initial mesh in order to reduce the computation cost.

Other authors [20] propose new formulations for the roundness index based on length measurements, surface area and volume. Based on the idea that the ratio between the volume and surface area reflects the roundness, this index is defined as:

$$\mathcal{R} = \frac{V}{S\sqrt[3]{abc}} \tag{3}$$

In this work, a specific software Pixform is used to compute it.

In another work [3], the roundness index is defined as:

$$\mathcal{R} = \frac{S}{4\pi(\frac{a+b+c}{6})^2} \tag{4}$$

i.e., as the ratio between the surface area of the particle and a sphere with a diameter equal to the arithmetic mean of the three length measurements, and it is computed from the voxel model.

There is a 3D approach based on ray-casting. Using spherical harmonics expansion, the roundness index is computed as a surface integral of the dot product between the surface position vector $\mathbf{r}$ and the unit normal vector to the surface $\mathbf{n}$, $\mathbf{r} \cdot \mathbf{n}$, [9]. However, the computation of this index is restricted to star-shaped particles.

In this paper, we present an efficient method to compute a 3D roundness index. It is based on a discretized model, the Extreme Vertices Model, follows a ray-casting approach based on distances and is not restricted to star-shaped particles.

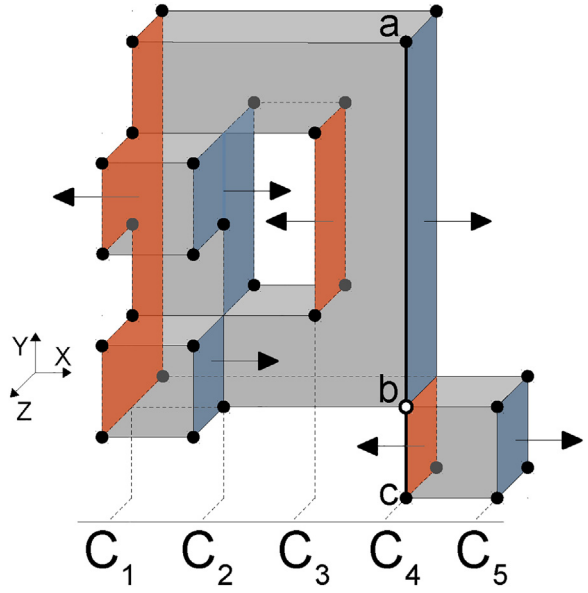


**Fig. 2.** An OPP with its *extreme vertices* marked with dots; a vertical *brink* from vertex **a** to vertex **c** is marked where these vertices are both *extreme vertices* while vertex **b** is not; cuts perpendicular to *X*-axis are shown with its corresponding faces in red and blue according to their orientation. (For interpretation of the references to colour in this figure legend, the reader is referred to the web version of this article.)

## 3. Extreme Vertices Model

The most common model to represent 3D binary digital images is the voxel model. The continuous analog of a 3D binary voxel model is an orthogonal pseudo-polyhedron (OPP) [27], i. e., an orthogonal polyhedron with a possible non-manifold boundary.

The Extreme Vertices Model is an alternative representation model for 3D binary digital images in which the object is represented by a subset of the corresponding OPP vertices, called extreme vertices.

Let $P$ be an OPP, a *brink* of $P$ is the maximal uninterrupted segment built out of a sequence of collinear and contiguous two-manifold edges of $P$. The brink ending vertices are called extreme vertices (*EV*). An OPP, and hence a 3D digital image, can be unambiguously represented by this *EV* set. A *cut* is the set of vertices lying on a plane perpendicular to a main axis of $P$. The Extreme Vertices Model (EVM) represents objects by the *EV* set, sorted lexicographically. Fig. 2 shows an example of an OPP. Extreme vertices are marked with a dot. There are only 4 vertices of the OPP that are not extreme vertices. Segment from vertex **a** to vertex **c** is a brink and therefore vertices **a** and **c** are extreme vertices while vertex **b** is not. Cuts perpendicular to the *X*-axis (from $C_1$ to $C_5$) are coloured. The different colors and corresponding arrows show faces perpendicular to the *X*-axis with its orientation.

EVM is a complete B-Rep model as all the geometry and neighboring information of faces, edges and vertices of the corresponding OPP can be obtained [43]. The storage requirements for an OPP $P$ in its EVM representation is $O(n)$, $n$ being the cardinality of the *EV* set which is $O(nv)$, $nv$ being the total number of vertices of the OPP. EVM is a more concise scheme than the voxel model and even than

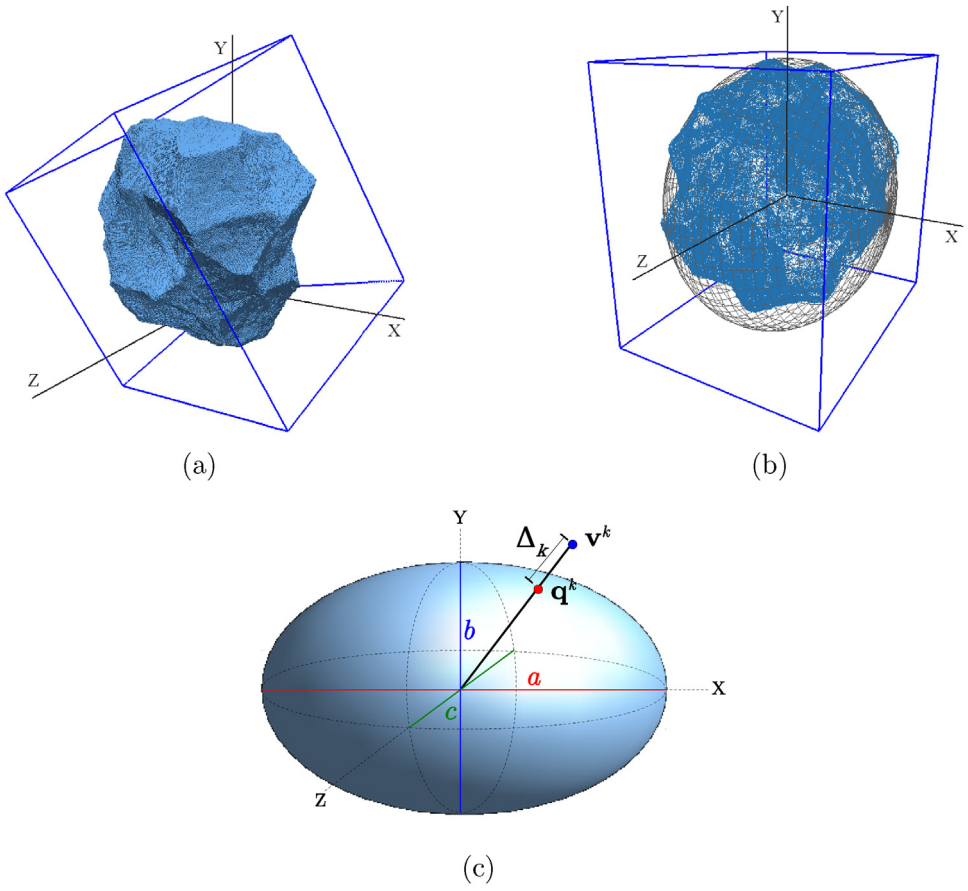


**Fig. 3.** (a) An object and its OBB. (b) Object and reference ellipsoid after applying the geometric transformation matrix that aligns and centers them with the frame of reference. (c) A ray through a point $v \in EV$, the intersection point between the ray and the ellipsoid $q$ and the difference $\Delta$.

models that store only boundary voxels as the semiboundary and shell models [37]. For more details concerning EVM see [2,37].

OPP have been used in several 3D applications as Boolean operations [8,17], direct skeleton computation (instead of iterative peeling techniques) [16,31], orthogonal hull computation [6,7] and in theory of hybrid systems to model the solutions of reachable states [8,13].

Concerning the EVM model the following operations have been developed: object volume and surface, and Boolean operations [1]; lossless model simplification [12]; morphological erosion and dilation operations and connected component labeling [36,38], and structural parameters computation as connectivity (genus) [11] and porosity with a virtual porosimetry method that doesn't need previous skeleton computation [38].

## 4. Indices computation

In this section, we present methods to compute the OBB and the corresponding length measurements as well as the sphericity and roundness indices of particles represented with EVM.

### 4.1. OBB computation

The method presented in this paper applies PCA to the set of extreme vertices, *EV*, of the EVM-represented object. Although the number of vertices of the EV set is significantly smaller than the number of voxels, the OBB produced from the EVM is very similar to the OBB produced from the voxel model and the computation time is greatly reduced in the EVM-based method. In Section 5 and Section 6 we discuss the results for both approaches applied to synthetic rock objects and real silica dataset, respectively.

### 4.2. Sphericity computation

The sphericity indices based on length measurements are obtained straightforward from the OBB.

To estimate the true sphericity index (Eq. (2)), the volume is computed from the EVM [1] giving the same result than computed from the voxel model. However, the surface area is computed from the voxel model with a method [46] that minimizes the mean square error. It performs a traversal of the boundary voxels assigning weights to them depending on its typology.

### 4.3. Roundness computation

Roundness can be estimated with a ray-casting-based approach. Uniformly distributed rays are traced from the center of the object to some sample points on its surface. For each ray, the difference between the distance from the center to the corresponding sample point and the radius of a reference shape at this point is computed. Then, roundness is estimated as an average of these distances.

Based on this idea, in this paper we propose a new 3D roundness index computation method. It uses the ellipsoid inscribed in the OBB of the object under consideration as a reference shape. The presented approach traces rays from the center of this ellipsoid to each vertex of the *EV* set in the EVM-represented object. For any vertex $\mathbf{v} \in EV$, the difference between the distance from the center to $\mathbf{v}$ and the radius of the ellipsoid passing through $\mathbf{v}$ are computed and the roundness index is obtained as the average of

these distances. The EVM-based roundness index is computed in four steps:

1. Compute the principal axes of the reference ellipsoid inscribed in the OBB of the object with the method presented in Section 4.1. See Fig. 3(a).
2. Compute a geometric transformation matrix, $M$, that aligns the OBB with the frame of reference and centers it at the origin $O$. Apply $M$ to each $\mathbf{v} \in EV$. See Fig. 3(b).
3. For each $\mathbf{v}^k \in EV$, trace a ray from the origin to $\mathbf{v}^k$, and compute the intersection point between this ray and the reference ellipsoid, $\mathbf{q}^k$, and the distance between $\mathbf{v}^k$ and $\mathbf{q}^k$, $\Delta_k$. The intersection point $\mathbf{q}^k$ can be obtained solving the quadratic equation $t^2|\mathbf{p}^k|^2 - 1 = 0$ for $t$, with $\mathbf{p}^k = (2v_1^k/a, 2v_2^k/b, 2v_3^k/c)$. See Fig. 3(c).
4. Compute the roundness $\mathcal{R}$ as the average of the previous computed distances. To remove the size effect, the average is divided by a normalization factor. We use the geometric mean of the principal axes lengths of the reference ellipsoid $(a, b, c)$. This is the same normalization factor applied in the method that will be used to compare the present EVM-based method [20], which have proven to have a strong correlation with Krumbein's roundness. The average is also multiplied by a factor of 10 to enhance the readability of the results. Finally, we subtract the result to 1 in order to keep the roundness definition, where 1 correspond to a perfectly round object and less than 1 for any other object. Finally, roundness $\mathcal{R}$ is expressed as:

$$\mathcal{R} = 1 - \frac{10}{n(abc)^{\frac{1}{3}}} \sum_{k=1}^{n} \Delta_k \tag{5}$$

where $n$ is the cardinality of $EV$.

Note that Eq. (5) can give negative values for non rock-like objects, which are not studied in this paper. On the other hand, the factor of 10 we apply does not affect the correlation formula, since it depends on the mean and the covariance of the data.

## 5. Results with synthetic data

This section and the following show a comparative between VXM-based methods and EVM-based methods in three experiments. The corresponding programs have been written in C++ and tested on a PC Intel® Core i7-4600M CPU@2.90GHz with 7.6 GB RAM and running Linux.

### 5.1. EVM-roundness correlation using Krumbein's chart

In order to show the correlation of the EVM-roundness index (Eq. (5)) with the roundness index defined by Wadell, the silhouettes of the Krumbein's chart (see Fig. 1) have been tested in a 2D version of the proposed method. Each tested image was created with a resolution of ≈320 × 320 pixels. Fig. 4 shows the relationship between Krumbein's roundness and EVM-roundness. These results have a linear correlation of 0.898. The EVM-roundness index has also been computed applying the OBB computed from the voxel model. It results in a slightly better (almost the same) correlation of 0.902.

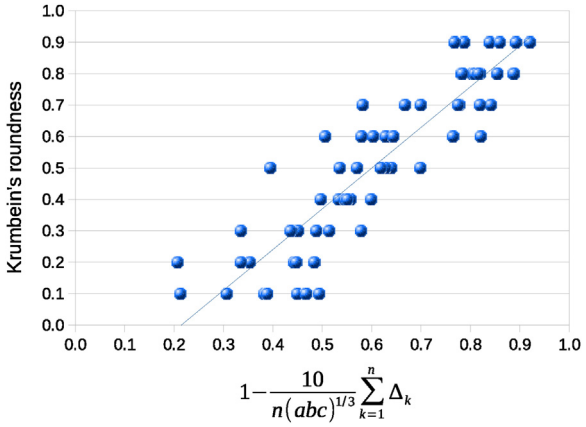


**Fig. 4.** Relationship between Krumbein's chart roundness and EVM-roundness (Eq. (5)).

### 5.2. Indices computation for synthetic rocks

We have used a GPL Blender extension, *rock Generator* (wiki.blender.org/index.php/Extensions:2.6), to create a set of thirty 3D models of rocks with different expected sphericity and roundness (see Fig. 5). These models simulate sedimentary rocks whose sizes can range from mm to hundredths of mm. Each model was converted to a voxel model with a resolution of ≈512 × 512 × 512 voxels. Distribution of the set of rocks according to their computed sphericity and roundness is shown in Fig. 6.

Statistics for the 30 rock datasets are listed in Table 1. For each dataset it shows the size in voxels, the number of used points to compute the VXM-based OBB and its volume. Next, it shows the same parameters for the EVM-based OBB. The last column shows the volume difference between both approaches.

From the results obtained in the 30 rock datasets we have observed that in 14 rocks (marked in bold in Table 1) the EVM-based OBB is tighter than the VXM-based OBB. Moreover, the volume difference between both approaches ranges from 0.10% (R6) to 2.63% (R2); in both cases the VXM-based OBB is tighter than EVM-

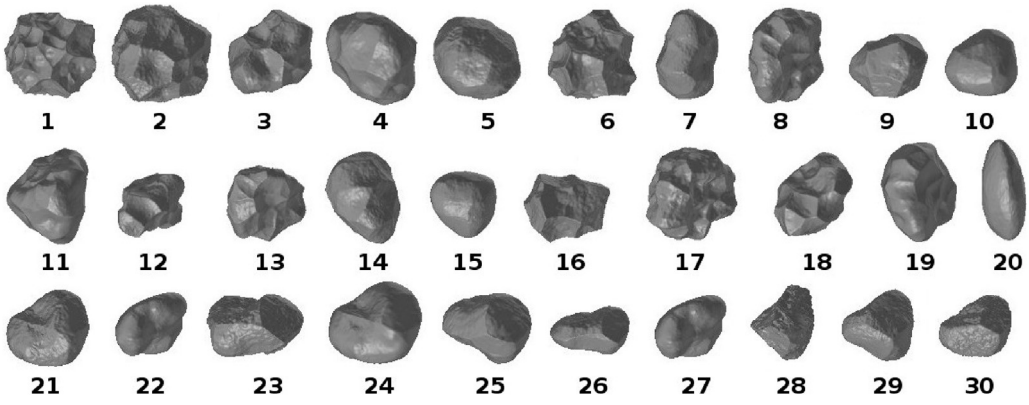


**Fig. 5.** Thirty 3D rock samples created with rockGenerator.

**Table 1**
Statistics of datasets for resolution 512 × 512 × 512.

| D. | Size | VXM | | EVM | | %v.d. |
|---|---|---|---|---|---|---|
| | | pts., $10^5$ | OBBVol, $10^6$ | pts., $10^3$ | OBBVol, $10^6$ | |
| **R1** | 485×512×508 | 483 | 157 | 592 | 153 | 2.47 |
| R2 | 495×512×506 | 554 | 132 | 652 | 135 | 2.63 |
| R3 | 511×465×510 | 502 | 107 | 577 | 109 | 1.73 |
| **R4** | 511×510×495 | 560 | 126 | 561 | 123 | 2.05 |
| **R5** | 485×485×512 | 596 | 123 | 535 | 123 | 1.02 |
| R6 | 512×396×491 | 349 | 106 | 461 | 106 | 0.10 |
| **R7** | 511×370×357 | 302 | 63 | 346 | 62 | 2.02 |
| **R8** | 511×409×402 | 349 | 79 | 434 | 78 | 0.80 |
| **R9** | 414×391×512 | 369 | 83 | 440 | 83 | 0.12 |
| R10 | 473×419×512 | 489 | 101 | 492 | 102 | 0.26 |
| **R11** | 511×507×422 | 424 | 103 | 502 | 103 | 0.27 |
| R12 | 420×512×441 | 342 | 105 | 419 | 108 | 2.01 |
| R13 | 495×466×512 | 404 | 98 | 525 | 100 | 2.57 |
| R14 | 511×504×417 | 478 | 99 | 492 | 100 | 1.02 |
| **R15** | 511×440×509 | 564 | 119 | 505 | 119 | 0.25 |
| R16 | 405×437×512 | 321 | 77 | 444 | 77 | 0.32 |
| **R17** | 484×512×475 | 440 | 119 | 533 | 116 | 2.59 |
| R18 | 511×475×482 | 460 | 116 | 510 | 118 | 2.04 |
| R19 | 512×410×389 | 340 | 75 | 386 | 77 | 2.54 |
| **R20** | 511×360×224 | 185 | 38 | 256 | 38 | 0.17 |
| R21 | 471×419×512 | 404 | 88 | 475 | 89 | 2.00 |
| R22 | 453×471×512 | 461 | 109 | 459 | 110 | 0.77 |
| **R23** | 334×385×512 | 278 | 66 | 360 | 65 | 2.28 |
| R24 | 451×426×512 | 385 | 86 | 470 | 87 | 1.93 |
| **R25** | 404×443×512 | 370 | 93 | 425 | 90 | 2.60 |
| R26 | 310×356×512 | 230 | 48 | 328 | 49 | 2.34 |
| R27 | 429×456×512 | 374 | 100 | 493 | 102 | 2.57 |
| **R28** | 511×466×432 | 301 | 79 | 451 | 78 | 2.13 |
| **R29** | 463×512×464 | 436 | 110 | 529 | 109 | 0.48 |
| R30 | 430×393×512 | 329 | 84 | 435 | 85 | 1.81 |
| Sph. | 512×512×512 | 698 | 134 | 575 | 134 | 0.04 |

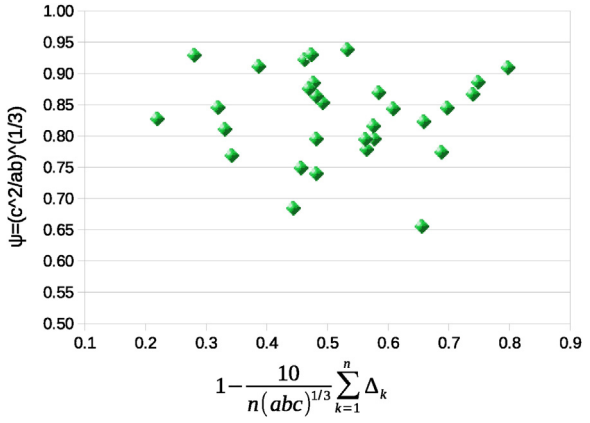


**Fig. 6.** Distribution of the rock samples according to their sphericity (Eq. (1) and roundness (Eq. (5)).

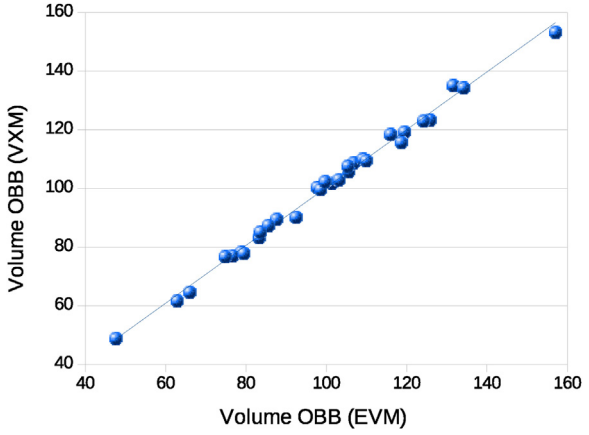


**Fig. 7.** Relationship between the OBB volume computed with VXM and EVM.

based OBB. The minimum and maximum differences considering the datasets in which the EVM-based OBB is tighter are 0.12% (R9) and 2.60% (R25) respectively. In the sphere dataset the VXM-based OBB is tighter than EVM-based OBB and the difference is just 0.04%.

Moreover, Fig. 7 shows the relationship between the OBB volume computed with VXM and EVM. These results have a strong correlation of 0.997. Therefore we conclude that the EVM-based OBB is, at least, as accurate as the VXM-based OBB.

Table 2 shows the sphericity and roundness indices computed from Eqs. (1) and (5) respectively. Next the times to compute: the EVM-based OBB, the EVM-roundness, the VXM-based OBB and the VXM-based surface area. In this case, the average time to compute the EVM-roundness and the VXM-roundness indices for the rock samples is 115 and 9592 ms respectively, i.e., our approach is more than an order of magnitude faster. This is mainly because we do not need to compute the surface area.

Our method has the disadvantage of the cost of conversion, the average time to convert VXM to EVM for the rocks samples is 13611 ms. However, we have developed an EVM-based platform which offers a series of operations for binary volumes. The cost of converting VXM a EVM is shared by all these processes. Besides the length measures, sphericity and roundness presented in this paper, other structural parameters can be computed faster than in their VXM-representation, such as the genus [5,11], the skeleton [31,32] and the pore-size distribution for porous materials [38].

The values of sphericity (Eq. (1)) and roundness (Eqs. (3) and (4)), based on length measurements will also be as accurate computed with VXM than computed with EVM and the resulting correlations

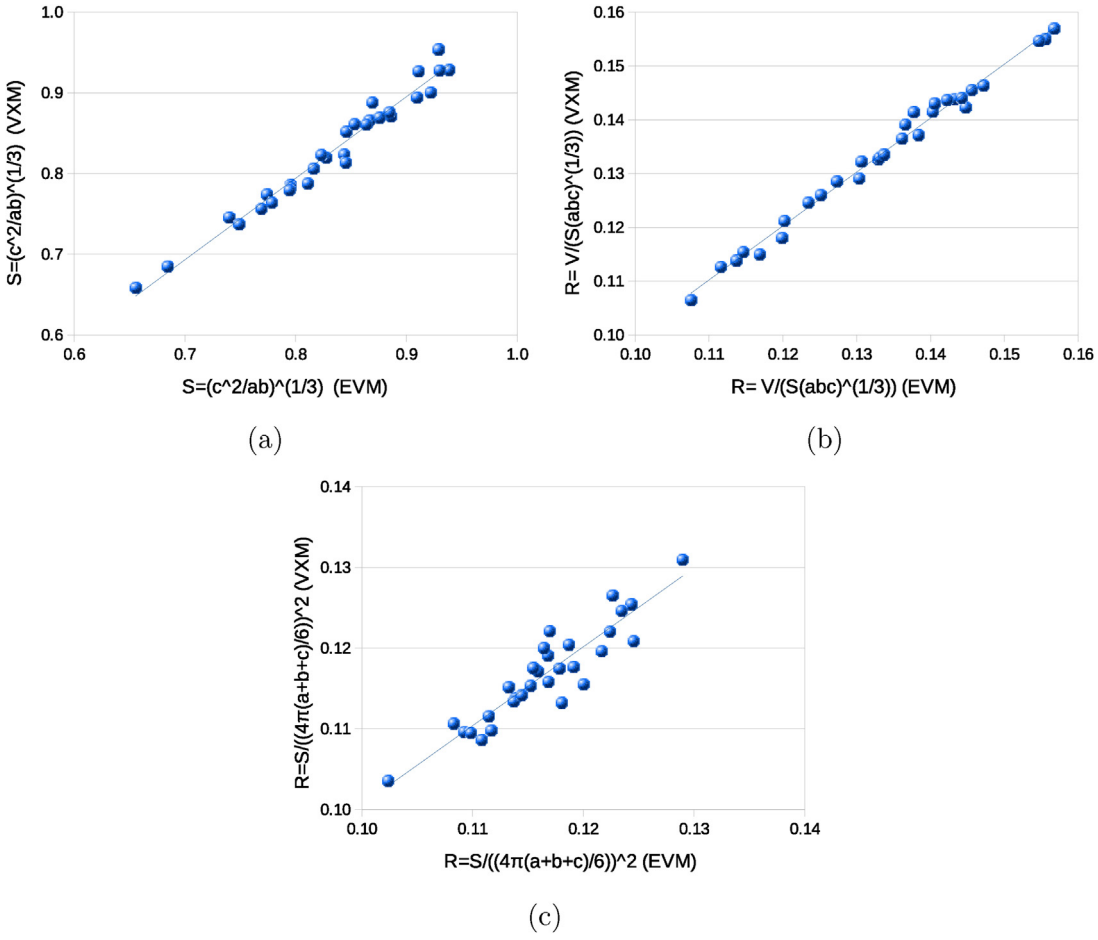


**Fig. 8.** Relationship between VXM and EVM in the computation of (a) sphericity Eq. (1), (b) roundness indices Eq. (3) and (c) Eq. (4).

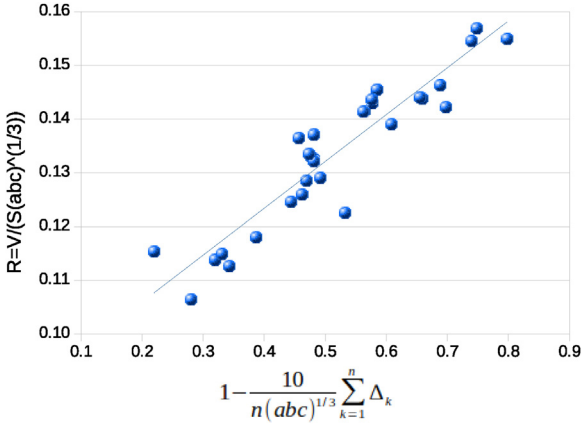


**Fig. 9.** Relationship between VXM-roundness (Eq. (3)) and EVM-roundness (Eq. (5)).

are 0.985, 0.995, and 0.922 respectively. Fig. 8 shows the graphs with these correlations.

Finally the VXM-roundness index (Eq. (3)) has been compared with the roundness index proposed (Eq. (5)). The correlation is 0.933 and the corresponding graph is shown in Fig. 9.

### 5.2.1. Resolution study

We also show that, the model resolution has little effect on the computation of the OBB, sphericity and roundness indices. For this study, we have selected six rocks and the sphere, which cover a wide range of sphericity and roundness indices (see Fig. 10). We have tested the selected models with space resolutions of $64 \times 64 \times 64$, $128 \times 128 \times 128$, $256 \times 256 \times 256$ and $512 \times 512 \times 512$. Fig. 11(a) shows, in a log–log scale, the volume difference computed between a VXM-based and an EVM-based OBB. Note that the volume difference decreases while resolution increases and that, even with a low resolution of $64 \times 64 \times 64$, the difference is less than 6%. Moreover, for some samples (R2,R12, and R19) the dependence is almost linear.

Fig. 11(b) shows, in a log–log scale, how resolution affects the computation time in both methods. From the analysis of these data it can be deduced that the VXM-based method is of cubic order ($cn^3$) whereas the EVM-based method is of quadratic order ($cn^2$) as they depend directly on the number of points in the respective representation.

Fig. 12(a) and (b) shows how resolution affects the computation of sphericity and roundness respectively using the proposed methods. We have computed the relative difference respect the model in the $512 \times 512 \times 512$ space resolution. Note that the sphericity index is almost invariant, in the worst tested case, the relative difference is less than 1%. Regarding the roundness index, in the worst tested case, the relative difference is less than 12%, this difference is bigger than that of the sphericity index due to EVM-roundness is highly dependent on the number of points. For instance, the R12 sample in the $64 \times 64 \times 64$ space resolution has just 1.5% of points that are in the $512 \times 512 \times 512$ space resolution. Therefore, this is a good result as the resolution in which real models are acquired is increasing constantly.

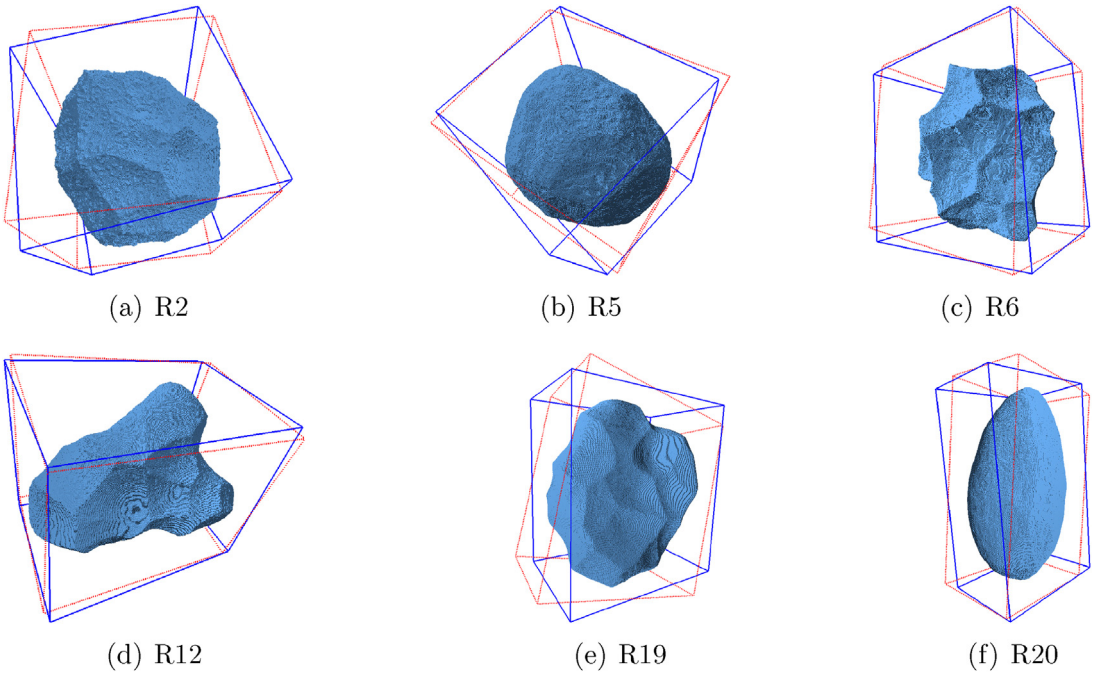


**Fig. 10.** Datasets of the 6 selected rocks and their OBB. The EVM-based and VXM-based OBB in continuous (blue) and stippled (red) line respectively. (For interpretation of the references to colour in this figure legend, the reader is referred to the web version of this article.)

**Table 2**
Results of datasets for resolution $512 \times 512 \times 512$.

| D. | $\Psi$ (Eq. (1)) | $\mathcal{R}$ (Eq. (5)) | Time (ms) | | | |
|---|---|---|---|---|---|---|
| | | | OBB-EVM | *R*-EVM | OBB-VXM | SA-VXM |
| R1 | 0.93 | 0.28 | 65 | 79 | 5088 | 8686 |
| R2 | 0.94 | 0.53 | 74 | 74 | 4646 | 8970 |
| R3 | 0.84 | 0.61 | 63 | 91 | 4641 | 7777 |
| R4 | 0.85 | 0.70 | 63 | 81 | 4951 | 8684 |
| R5 | 0.91 | 0.80 | 59 | 72 | 4289 | 8591 |
| R6 | 0.85 | 0.32 | 51 | 64 | 3046 | 5607 |
| R7 | 0.77 | 0.69 | 43 | 50 | 2460 | 4628 |
| R8 | 0.74 | 0.48 | 48 | 59 | 3465 | 5413 |
| R9 | 0.87 | 0.58 | 49 | 60 | 3434 | 5755 |
| R10 | 0.89 | 0.75 | 54 | 66 | 4036 | 6993 |
| R11 | 0.88 | 0.48 | 54 | 69 | 3480 | 6387 |
| R12 | 0.83 | 0.22 | 46 | 59 | 3030 | 5528 |
| R13 | 0.68 | 0.44 | 63 | 69 | 3583 | 6630 |
| R14 | 0.82 | 0.66 | 57 | 65 | 3294 | 6701 |
| R15 | 0.87 | 0.74 | 56 | 66 | 3651 | 7749 |
| R16 | 0.92 | 0.46 | 48 | 61 | 2647 | 4935 |
| R17 | 0.81 | 0.33 | 59 | 71 | 4047 | 6697 |
| R18 | 0.80 | 0.48 | 55 | 67 | 4410 | 7200 |
| R19 | 0.78 | 0.56 | 44 | 53 | 2927 | 5097 |
| R20 | 0.66 | 0.66 | 28 | 35 | 1494 | 2711 |
| R21 | 0.80 | 0.58 | 52 | 64 | 3447 | 6101 |
| R22 | 0.75 | 0.46 | 49 | 62 | 3690 | 7031 |
| R23 | 0.85 | 0.49 | 39 | 47 | 2155 | 3876 |
| R24 | 0.82 | 0.58 | 51 | 62 | 3242 | 5662 |
| R25 | 0.86 | 0.48 | 46 | 51 | 3063 | 5324 |
| R26 | 0.79 | 0.56 | 35 | 43 | 1802 | 3356 |
| R27 | 0.77 | 0.34 | 55 | 65 | 3375 | 6141 |
| R28 | 0.91 | 0.39 | 49 | 59 | 3091 | 5189 |
| R29 | 0.93 | 0.47 | 58 | 69 | 3790 | 6363 |
| R30 | 0.88 | 0.47 | 47 | 60 | 2727 | 4964 |
| Sph. | 1.00 | 0.99 | 63 | 76 | 4708 | 9649 |

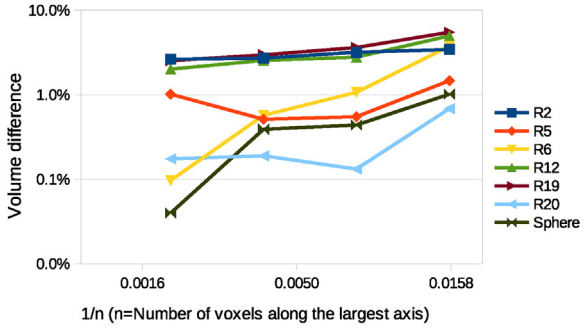


(a) Volume difference in a log-log scale.

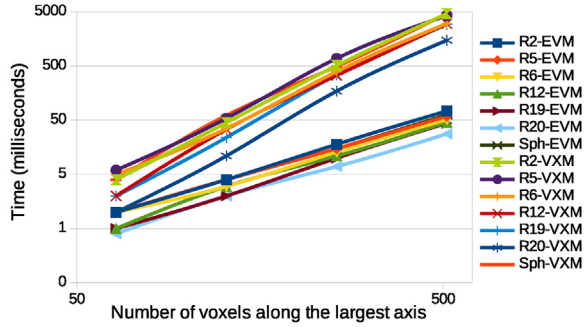


(b) Computation time in a log-log scale.

**Fig. 11.** Resolution test for OBB computation: volume difference and computation time.

## 6. Analysis of a real silicon nanocrystals dataset

A real silicon nanocrystals (Si NCs) dataset has been obtained. In this section we use this dataset to compare values obtained with EVM-based and with VXM-based approaches.

A more detailed discussion on the NCs sample growth, the acquisition EFTEM method and the results obtained using the VXM-based approach can be found in [23] which are also briefly included in this section.

Concerning this application, the contribution of this paper is the comparison of values obtained with EVM-based and with VXM-

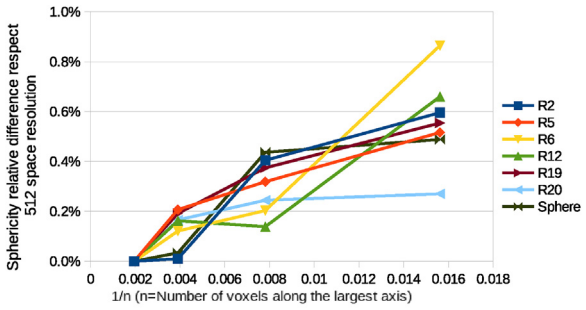


(a) Sphericity

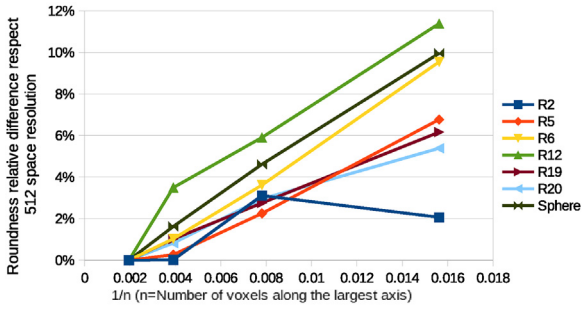


(b) Roundness

**Fig. 12.** Resolution test for OBB computation: sphericity and roundness variation.

based approaches. Moreover we also describe in detail the required preprocessing to convert the raw format tomography into a suitable VXM model.

### 6.1. Sample acquisition and preprocessing

Size controlled Si NCs embedded in a $SiO_2$ matrix were grown on Si substrates by thermal evaporation of a superlattice comprised of 20 $SiO_2/SiO_{x=1.2}$ bilayer stacks and a 10 nm thick capping oxide [22]. The sample has 3 nm thick $SiO_x$ layers and 5 nm thick $SiO_2$ spacing layers.

EFTEM (energy filtered transmission electron microscopy) was performed and tilt series from $-68^\circ$ to $+76^\circ$ at an increment of $4^\circ$ were acquired [21,47]. Due to the limited tilt range, objects appear elongated along the *Y*-direction in the tomographic reconstruction. The elongation factor can be estimated from the tilt range and is $\approx$1.3 for the conditions specified above. From the complete image we have considered the undisturbed 10 first layers as the few NCs in the topmost layers maybe some specimen preparation artefact. Therefore the final considered sample size is $49 \times 106 \times 157$ nm.

The complete tomography is a 32-bit gray scale dataset in RAW format and size $131 \times 281 \times 332$. The 3D projection and some 2D slices of this dataset are depicted in Fig. 13.

The following preprocessing steps have been applied:

1. Convert the original dataset to a 8-bit voxel model.
2. Scale the voxel model via trilinear interpolation, to twice its size in order to better define the grain shapes.
3. Apply an elongation factor of 1.3 to the *Y* axis: $262 \times 730 \times 664$ voxel model.
4. Crop the model in order to remove the base plate and consider only the 10 first layers: $262 \times 730 \times 286$ voxel model
5. Apply a binary threshold filter.
6. Remove noise applying morphological opening and closing operations

Step 5 requires a threshold that allows yielding a good segmentation of the particles. The gray value histogram is shown in Fig. 14, in this case, high values of gray represent the foreground and the curve helps to determine where the background ends and the foreground begins. Note that the curve falls off around the value of 50. Therefore, thresholds of 45, 50 and 55 have been used to binarize the dataset.

Fig. 15 shows the sample after the corresponding threshold and noise removal, where for each threshold, the number of connected components (CC), considering 6-connectivity, is indicated. Observe that the result of applying a threshold of 45 looks like a model having several agglomerated particles. The result of applying a threshold of 55 seems to lose information. Therefore, we consider that the particle shapes are better defined applying a threshold of 50.

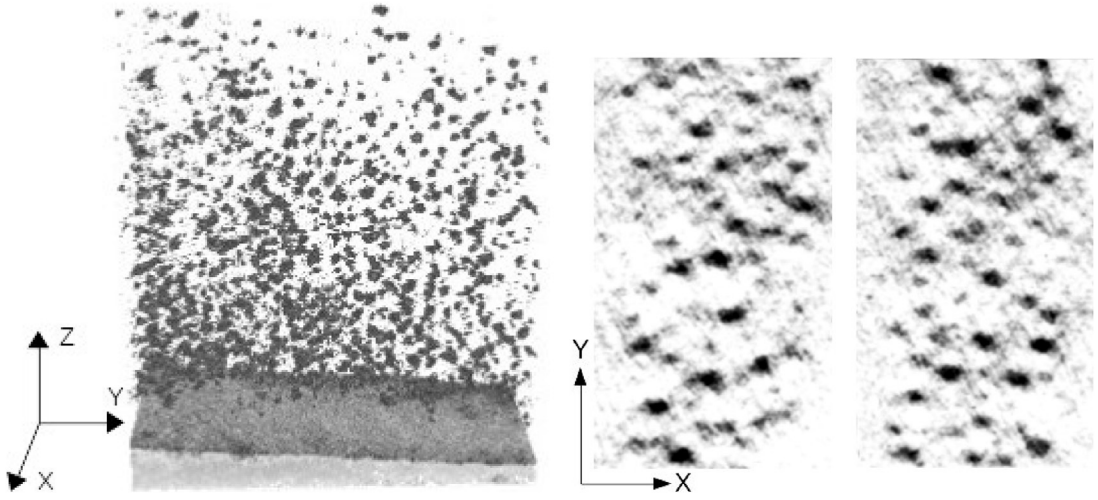


(a) 3D projection (b) 2D slices

**Fig. 13.** Some views of the silicon nanocrystals dataset tomography.

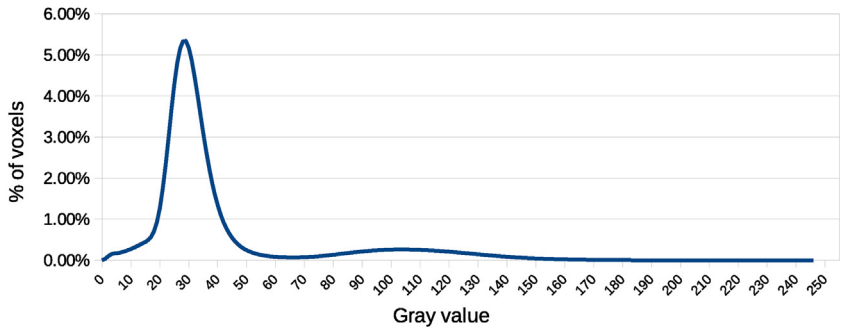


**Fig. 14.** Gray value histogram of the sample.

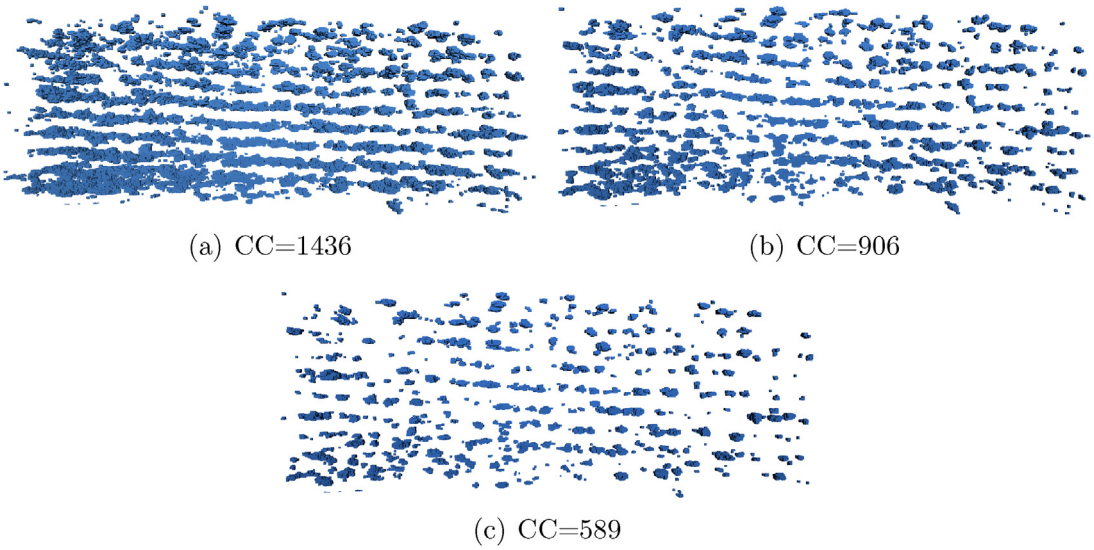


**Fig. 15.** Dataset after segmentation and noise removal with thresholds (a) 45, (b) 50 and (c) 55.

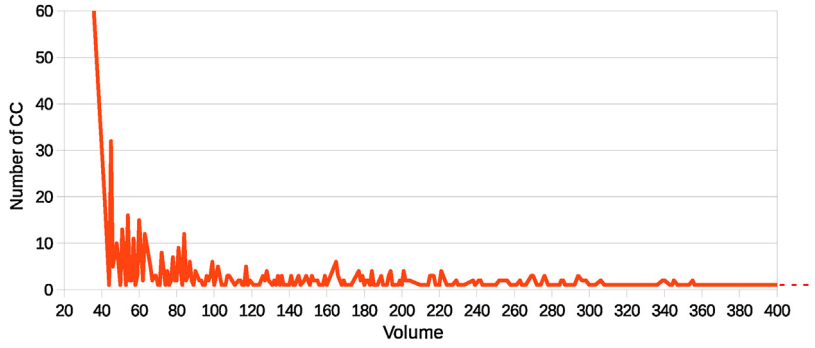


**Fig. 16.** Number of connected components according to their volumes.

After the preprocessing, we compute the connected components, which represent the quantum dot particles. Fig. 16 shows a graph of the number of CC according to their volumes.

From the previous data, a voxel size of 0.19 nm approx results. The average size of a particle (diameter) is expected to be around 2 nm or 3 nm. Considering spherical particles this size would correspond to 1190 voxels approx. However, for the size distribution computation, only particles with a volume of 200 or more voxels will be considered. Therefore, the resulting dataset consists of 496 CC. See Fig. 17 where the resulting particles are depicted.

### 6.2. Particles properties computation

Results obtained using the VXM-based approach [23] showed that NCs in superlattices are non-agglomerated, individual clusters with slightly oblate spheroidal shape. Length measurements and sphericity computation were used for these conclusions which were validated by the NCs experts. Now we show the obtained values using the VXM and EVM approaches.

One of the studied shape parameters was the mean diameter computed as $(a+b+c)/3$. The value obtained with EVM and VXM were 2.72 nm and 2.67 nm respectively. Both values fit very well to the photoluminescence results [22] and the fact that the original $SiO_x$-layer from which the Si NCs formed was 3 nm thick.

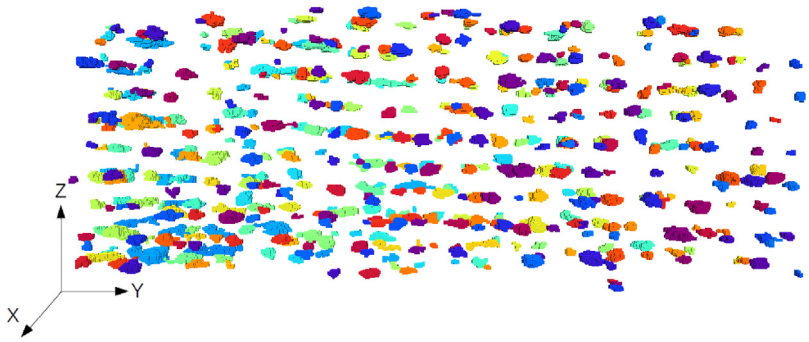


**Fig. 17.** Resulting particles with volume larger than 200 voxels.

Ratios $c/a$, $c/b$ and $a/b$ have also been computed. From our understanding the NCs are not perfectly spherical but a bit like a rotational ellipsoid with the lateral shape quite circular since the nanocrystals have no restrictions in X-Y direction and these lateral dimensions are larger than the vertical dimension ($Z$) due to the self-organized growth with the limiting upper and lower $SiO_2$ barrier. The obtained average ratios with VXM were $c/a = 0.41$, $c/b = 0.61$ and $a/b = 1.48$, and with EVM were $c/a = 0.42$, $c/b = 0.61$ and $a/b = 1.45$. These values corroborate the previous assumption. Moreover a mean $c/b$ of 0.61 corresponds to a an oblate spheroid with just 12% more surface-to-volume ratio than a real sphere.

The true sphericity (Eq. (2)) has only been computed with VXM and the obtained value of 0.80 as average with a peak value of 0.86 in the normal distribution is a good result, as there are almost no perfectly spherical NCs with $\Psi = 1.0$, but only few have significantly small $\Psi$-values.

The average sphericity based on length measurements $a, b, c$ (Eq. (1)) gives a different value than the true sphericity but the values obtained with the two compared approaches are very similar: 0.64 (VXM) and 0.65 (EVM).

Roundness is not a really useful parameter for this NC application, since the scale in which these sharp or round edges are, is at sub-nanometer level, i.e. close to or even beyond the resolution limit of EFTEM tomography. However, in order to further test the EVM-based presented approach we have computed the roundness using VXM (Eq. (3)) and EVM (Eq. (5)) and the obtained values are also very similar: 0.15 and 0.16 respectively.

## 7. Conclusions

We have presented new methods based on EVM to compute length measurements, sphericity and roundness of 3D objects represented as binary volume datasets.

Length measurements have been computed from the OBB of the object obtained by PCA applied to the restricted set of vertices of the EVM representation. Experimental results have shown that this method is as accurate as the same method with VXM and is more than an order of magnitude faster.

We have proposed a new EVM-based roundness index. The method to compute it is based on the ray-tracing paradigm and uses the vertices of the EVM representation. Besides, the time to compute the proposed index is also more than an order of magnitude faster compared with previous VXM-based methods, which depend on the surface area computation.

We have computed the correlation between our approach and the approach based on the voxel model for two sphericity indices and for the roundness index obtaining good results.

One of the advantages of EVM is that the cost of most of the involved processes are less affected by the increasing resolution than in VXM. We have corroborated this fact for the computation of the sphericity and roundness indices: the EVM approach is of quadratic order while the VXM is of cubic order with increasing resolution.

A complete study of a Si NCs dataset has been presented and the computed parameters are equally accurate using VXM or EVM while the computation time is reduced by an order of magnitude.

As a future work, we are devising an alternative method to estimate the real surface area directly of an EVM-represented object so that we could compute the true sphericity without using a VXM-based scheme. We are also studying a method to partition the pore space (for porous materials) without having to compute the skeleton.

## Acknowledgements

We gratefully acknowledge Lena F. Kourkoutis (Cornell University) for EFTEM tomography. This work was partially supported by the national Project TIN2011-24220 of the Spanish government. The authors thank the anonymous reviewers whose suggestions and questions gave them challenge and opportunity to greatly improve the paper.

## References

[1] A. Aguilera, Orthogonal Polyhedra: Study and Application, LSI-Universitat Politècnica de Catalunya, 1998, Ph.D. thesis.
[2] A. Aguilera, D. Ayala, Orthogonal polyhedra as geometric bounds in constructive solid geometry, in: Fourth ACM Symposium on Solid Modeling and Applications, ACM, 1997, pp. 56–67.
[3] K. Alshibli, A. Druckrey, R. Al-Raoush, T. Weiskittel, N. Lavrik, Quantifying morphology of sands using 3D imaging, ASCE J. Mater. Civil Eng. 27 (2015), 04014275-1–04014275-10.
[4] D. Asahina, M. Taylor, Geometry of irregular particles: direct surface measurements by 3D laser scanner, Powder Technol. 213 (2011) 70–78.
[5] D. Ayala, E. Vergés, I. Cruz, A polyhedral approach to compute the genus of a volume dataset, GRAPP/IVAPP (2012) 38–47.
[6] T. Biedl, B. Genç, Reconstructing orthogonal polyhedra from putative vertex sets, Comput. Geometry 44 (2011) 409–417.
[7] A. Biswas, P. Bhowmick, M. Sarkar, B.B. Bhattacharya, A linear-time combinatorial algorithm to find the orthogonal hull of an object on the digital plane, Inform. Sci. 216 (2012) 176–195.
[8] O. Bournez, O. Maler, A. Pnueli, Orthogonal polyhedra: representation and computation, in: Hybrid Systems: Computation and Control. LNCS 1569, Springer, 1999, pp. 46–60.
[9] J. Bullard, E.J. Garbozzi, Defining shape measures for 3D star-shaped particles: sphericity, roundness, and dimensions, Powder Technol. 249 (2013) 241–252.
[10] I. Cruz-Matías, Contribution to Structural Parameters Computation: Volume Models and Methods, Universitat Politécnica de Catalunya, 2014, Ph.D. Thesis.
[11] I. Cruz-Matías, D. Ayala, An efficient alternative to compute the genus of binary volume models, in: Proc. Int. Conf. GRAPP 2013, SciTePress, 2013, pp. 18–26.
[12] I. Cruz-Matías, D. Ayala, A new lossless orthogonal simplification method for 3D objects based on bounding structures, Graph. Models 76 (2014) 181–201.
[13] T. Dang, O. Maler, Reachability analysis via face lifting, in: Hybrid Systems: Computation and Control, Springer, 1998, pp. 96–109.
[14] G. Drevin, L. Vincent, Granulometric determination of sedimentary rock particle roundness, Proceedings of International Symposium on Mathematical Morphology (ISMM) (2002) 315–325.

[15] A. Eljarrat, L. López-Conesa, J. López-Vidrier, S. Hernández, B. Garrido, C. Magen, F. Peiró, S.E, Retrieving the optoelectronic properties of silicon nanocrystals embedded in a dielectric matrix by low-loss EELS, Nanoscale 6 (2014) 11911.
[16] D. Eppstein, E. Mumford, Steinitz theorems for orthogonal polyhedra, in: Proceedings of the 2010 Annual Symposium on Computational Geometry, ACM, 2010, pp. 429–438.
[17] C. Esperança, H. Samet, Vertex representations and their applications in computer graphics, Vis. Comput. 14 (1998) 240–256.
[18] G.V. Eyndhoven, M. Kurttepeli, C.V. Oers, P. Cool, S. Bals, K. Batenburg, J. Sijbers, Pore reconstruction and segmentation (PORES) method for improved porosity quantification of nanoporous materials, Ultramicroscopy 148 (2015) 10–19.
[19] S. Gutsch, D. Hiller, J. Laube, M. Zacharias, C. Kübel, Observing the morphology of single-layered embedded silicon nanocrystals by using temperature-stable tem membranes, Beilstein J. Nanotechnol. 6 (2015) 964–970.
[20] Y. Hayakawa, T. Oguchi, Evaluation of gravel sphericity and roundness based on surface-area measurement with a laser scanner, Comput. Geosci. 31 (2005) 735–741.
[21] S. Hernández, J. López-Vidrier, L. López-Conesa, D. Hiller, S. Gutsch, J. Ibá nez, S. Estradé, F. Peiró, M. Zacharias, B. Garrido, Determining the crystalline degree of silicon nanoclusters/$SiO_2$ multilayers by Raman scattering, J. Appl. Phys. 115 (2014) 203504.
[22] D. Hiller, S. Goetze, F. Munnik, M. Jivanescu, J.W. Gerlach, J. Vogt, E. Pippel, N. Zakharov, A. Stesmans, M. Zacharias, Nitrogen at the Si-nanocrystal/$SiO_2$ interface and its influence on luminescence and interface defects, Phys. Rev. B 82 (2010) 195401.
[23] D. Hiller, S. Gutsch, J. López-Vidrier, M. Zacharias, S. Estradé, F. Peiró, I. Cruz-Matías, D. Ayala, Determination of shape and sphericity of silicon quantum dots imaged by eftem-tomography, Phys. Status Solidi C 14 (2017) 1700216.
[24] J. Fonseca, M.C, C. O'Sullivan, P. Lee, Non-invasive characterization of particle morphology of natural sands, Soils Foundations 52 (2012) 712–722.
[25] L.F. Kourkoutis, X. Hao, S. Huang, B. Puthen-Veettil, G. Conibeer, M.A. Green, I. Perez-Wurfl, Three-dimensional imaging for precise structural control of Si quantum dot networks for all-Si solar cells, Nanoscale 5 (2013) 7499–7504.
[26] W.C. Krumbein, Measurement and geological significance of shape and roundness of sedimentary particles, J. Sedimen. Res. 11 (1941) 64–72.
[27] J. Lachaud, A. Montanvert, Continuous analogs of digital boundaries: a topological approach to iso-surfaces, Graph. Models 62 (2000) 129–164.
[28] J. Laube, S. Gutsch, D. Wang, C. Kübel, M. Zacharias, D. Hiller, Two-dimensional percolation threshold in confined Si nanoparticle networks, Appl. Phys. Lett. 108 (2016), 043106-1 - 043106-5.
[29] C. Lin, J. Miller, 3D characterization and analysis of particle shape using X-ray microtomography (XMT), Powder Technol. 154 (2005) 61–69.
[30] E. Martín-Badosa, A. Elmoutaouakkil, S. Nuzzo, D. Amblard, L. Vico, F. Peyrin, A method for the automatic characterization of bone architecture in 3D mice microtomographic images, Comput. Med. Imag. Graph. 27 (2003) 447–458, URL: smb://movibio.lsi.upc.edu/movibio/articles/repositori/MEN03.pdf.
[31] J. Martínez, N. Pla, M. Vigo, Skeletal representations of orthogonal shapes, Graph. Models 75 (2013) 189–207.
[32] J. Martínez Bayona, M. Vigo Anglada, N. Pla García, M.D. Ayala Vallespí, Skeleton computation of an image using a geometric approach, in: EUROGRAPHICS'10. Norrköping, Sweden, 2010, pp. 13–16.
[33] P.-E. Øren, S. Bakke, Reconstruction of Berea sandstone and pore-scale modelling of wettability effects, Jo. Petrol. Sci. Eng. 39 (2003) 177–199.
[34] L. Paavolainen, E. Acar, U. Tuna, S. Peltonen, T. Moriya, P. Soonsawad, V. Marjomäki, R.H. Cheng, U. Ruotsalainen, Compensation of missing wedge effects with sequential statistical reconstruction in electron tomography, PLoS One 9 (2014).
[35] L. Rico, A. Naranjo, S. Noriega, E. Martínez, L. Vidal, Effect of cutting parameters on the roundness of cylindrical bars turned of 1018 steel, Measurements (2010).
[36] J. Rodríguez, D. Ayala, Fast neighborhood operations for images and volume data sets, Comput. Graph. 27 (2003) 931–942, http://dx.doi.org/10.1016/j.cag.2003.08.015.
[37] J. Rodríguez, D. Ayala, A. Aguilera, Geometric Modeling for Scientific Visualization, in: EVM: A Complete Solid Model for Surface Rendering, Springer-Verlag, 2004, pp. 259–274.
[38] J. Rodríguez, I. Cruz, E. Vergés, D. Ayala, A connected-component-labeling-based approach to virtual porosimetry, Graph. Models 73 (2011) 296–310.
[39] T. Roussillon, H. Piégay, I. Sivignon, L. Tougne, F. Lavigne, Automatic computation of pebble roundness using digital imagery and discrete geometry, Comput. Geosci. 35 (2009) 1992–2000.
[40] M. Schroth, J. Istok, S. Ahearn, J. Selker, Characterization of miller-similar silica sands for laboratory hydrologic studies, Soil Sci. Soc. Am. J. 60 (1996) 1331–1339.
[41] E.D. Sneed, R.L. Folk, Pebbles in the lower Colorado river, Texas: a study in particle morphogenesis, J. Geol. (1958) 114–150.
[42] W. Sun, B. Starly, J. Nam, A. Darling, Bio-CAD modeling and its applications in computer-aided tissue engineering, Comput. Aided Des. 37 (2005) 1097–1114.
[43] M. Vigo, N. Pla, D. Ayala, J. Martínez, Efficient algorithms for boundary extraction of 2D and 3D orthogonal pseudomanifolds, Graph. Models 74 (2012) 61–74.
[44] H. Wadell, Volume, shape, and roundness of rock particles, J. Geol. 40 (1932) 443–451.
[45] H. Wadell, Sphericity and roundness of rock particles, J. Geol. 41 (1933) 310–331.
[46] G. Windreich, N. Kiryati, G. Lohmann, Voxel-based surface area estimation: from theory to practice, Pattern Recogn. 36 (2003) 2531–2541.
[47] A. Yurtsever, M. Weyland, D.A. Muller, Three-dimensional imaging of non-spherical silicon nanoparticles embedded in silicon oxide by plasmon tomography, Appl. Phys. Lett. 89 (2006) 151920.
[48] A. Zelenina, S. Dyakov, D. Hiller, S. Gutsch, V. Trouillet, M. Bruns, S. Mirabella, P. Löper, L. López-Conesa, J. López-Vidrier, S. Estradé, F. Peiró, B. Garrido, J. Bläsing, A. Krost, D. Zhigunov, M. Zacharias, Structural and optical properties of size controlled Si nanocrystals in $Si_3N_4$ matrix: the nature of photoluminescence peak shift, J. Appl. Phys. 114 (2013) 184311.
[49] B. Zhao, J. Wang, 3D quantitative shape analysis on form, roundness and compactness with $\mu$CT, Powder Technol. 291 (2016) 262–275.
[50] J. Zheng, R. Hryciw, Traditional soil particle sphericity, roundness and surface roughness by computational geometry, Géotechnique 65 (2015) 494–506.
[51] B. Zhou, J. Wang, B. Zhao, Micromorphology characterization and reconstruction of sand particles using micro X-ray tomography and spherical harmonics, Eng. Geol. 184 (2015) 126–137.

**Irving Cruz-Matí as** is full time professor in the Computer Science Department at University of Monterrey, Mexico. He received the Ph.D. in Computing from the Polytechnic University of Catalonia, Barcelona, Spain in 2014. His research interests include modelling, analysis and visualization of 3D biomedical samples, digital image processing and in general, the application of computer graphics in the bioengineering field.

**Dolors Ayala** is an Associate Professor of the Software Department of the Polytechnical University of Catalonia (UPC) and member of the Research Center of Biomedica Engineering of the UPC. She obtained a degree in Industrial Engineering (1982) and a PhD in Computer Science (1987). Her research interests are focussed in volume models and analysis techniques applied to the bioengineering discipline. She works in multidisciplinary projects with biomaterials, veterinary and geology researches. She publishes regularly in computer graphics journals and conferences.

**Daniel Hiller** studied physics at the University of Leipzig, Germany. He received his PhD from the University of Freiburg, Germany in 2011 with a thesis about defects in $SiO_2$-embedded Si nanocrystals. After that he became group leader and studied the doping properties of Si-nanocrystals. Currently he is a Feodor-Lynen-Fellow (Alexander-von-Humboldt Foundation) at the Australian National University and investigates ALD-based passivating carrier-selective contact materials for high-efficiency Si-photovoltaics.

**Sebastian Gutsch** is a postdoctoral researcher in the University of Freiburg, Germany. He received his PhD from the University of Freiburg, Germany in 2014. His research interests are focused in nanotechnology, quantum theory, transport, and material characterization.

**Margit Zacharias** studied Physics at the University of Leipzig. She got her PhD in Electrical Engineering (1984) and the habilitation in Experimental Physics (1999) at the University of Magdeburg. In 2000 she got a C3 group at the MPI for Microstructure Physics. She initiated the SPP 1165 on Nanowires in Germany. In 2006 she joint the University of Paderborn as Professor (Applied Physics), and in 2007 the University of Freiburg as Professor for Nanotechnology. From 2014–18 she was Vice President for Innovation and Technology Transfer. She is author and co-author of more than 260 papers and works with in material science and nanomaterials.

**Sònia Estradé** holds a bachelor's degree in Physics (2005), a master's degree in nanoscience and nanotechnology (2007) and a PhD. in nanosciences (2009) from the University of Barcelona. Lecturer of the Department of Electronics of UB since 2014. Specialist in electron energy loss spectroscopy (EELS) and in Transmission Electronic Microscopy (TEM), she develops her research work in the LENS-MIND group of the Department of Electronics. She is a member of the Institute of Nanoscience and Nanotechnology of the UB (IN2UB).

**Francesca Peiró** is the leader of the Laboratory of Electron Nanoscopies (LENS-MIND) (www.lens.el.ub.edu), full professor of the Department of Electronics and Biomedical Engineering at the University of Barcelone and researcher at the Nanoscience and Nanotechnology Institute (In2UB). She is also member of the Executive Board of the Spanish Society of Microscopy. The main objective of LENS is the development of instrumental methods as well as data treatment for advanced scientific problems in nanomaterials using Transmission Electron Microscopy and related analytical techniques.